

Transparent Porous ZnO|Metal Complex Nanostructured Materials: Application to Electrocatalytic CO 2 Reduction

Julian Guerrero, Nathanaelle Schneider, Fabienne Dumoulin, Daniel Lincot, Umit Isci, Negar Naghavi, Marc Robert

▶ **To cite this version:**

Julian Guerrero, Nathanaelle Schneider, Fabienne Dumoulin, Daniel Lincot, Umit Isci, et al.. Transparent Porous ZnO|Metal Complex Nanostructured Materials: Application to Electrocatalytic CO 2 Reduction. ACS Applied Nano Materials, 2023, 6 (12), pp.10626-10635. 10.1021/acsanm.3c01591 . hal-04158858

HAL Id: hal-04158858
https://cnrs.hal.science/hal-04158858

Submitted on 11 Jul 2023

HAL is a multi-disciplinary open access archive for the deposit and dissemination of scientific research documents, whether they are published or not. The documents may come from teaching and research institutions in France or abroad, or from public or private research centers.

L'archive ouverte pluridisciplinaire **HAL**, est destinée au dépôt et à la diffusion de documents scientifiques de niveau recherche, publiés ou non, émanant des établissements d'enseignement et de recherche français ou étrangers, des laboratoires publics ou privés.

This document is confidential and is proprietary to the American Chemical Society and its authors. Do not copy or disclose without written permission. If you have received this item in error, notify the sender and delete all copies.

Transparent hybrid materials (metal complexes/ZnO nanostructures): synergetic effects in electrocatalytic reactions, application to CO2 reduction

Journal:	*ACS Applied Nano Materials*
Manuscript ID	an-2023-015912
Manuscript Type:	Article
Date Submitted by the Author:	10-Apr-2023
Complete List of Authors:	Guerrero, Julian; University of Paris, Chemistry; IPVF Schneider, Nathanaelle; IPVF Dumoulin, Fabienne; Acibadem Universitesi, Biomedical Engineering Department Lincot, Daniel; IPVF Isci, Umit; Marmara University, Department of Metallurgical & Materials Engineering Naghavi, Negar; CNRS, E2P2L, UMI 3464 Robert, Marc; University of Paris, Chemistry

SCHOLARONE™
Manuscripts

Transparent hybrid materials (metal complexes/ZnO nanostructures): synergetic effects in electrocatalytic reactions, application to CO_2 reduction

Julian Guerrero,[a,b] *Nathanaelle Schneider,*[b] *Fabienne Dumoulin,*[c] *Daniel Lincot,*[b] *Umit Isci,*[d*] *Negar Naghavi,*[b*] *Marc Robert*[a,e*]

[a] Laboratoire d'Electrochimie Moléculaire, Université de Paris, CNRS, F-75006 Paris, France

[b] Institut Photovoltaïque d'Île-de-France (IPVF), CNRS, UMR 9006, 91120 Palaiseau, France

[c] Acıbadem Mehmet Ali Aydınlar University, Faculty of Engineering and Natural Sciences, Biomedical Engineering Department, 34752 Ataşehir, Istanbul, Türkiye

[d] Marmara University, Faculty of Technology, Department of Metallurgical & Materials Engineering, 34722 Istanbul, Türkiye

[e] Institut Universitaire de France (IUF), F-75005, Paris, France

Abstract

We developed a simple and versatile approach for the electrochemical growth of hybrid ZnO/molecular catalyst nanostructured layers. A metal oxide/catalyst hybrid nanoporous layer with a sponge-like structure at the nanoscale and multiscale 3D hierarchical structures based on nanoporous ZnO layers grown on zinc oxide nanorods have been obtained. The thickness and structure of the hybrid nanoporous layer as well as the catalyst concentration can be tuned. This method allowed for the introduction of water soluble molecular catalysts based on porphyrin and/or phthalocyanine derivatives into the ZnO matrix with a homogeneous distribution of the complex. As an illustrative example, combining hybrid ZnO with a very low concentration of an encapsulated Co-based molecular catalyst inside the oxide layer resulted in a 97% catalytic response toward CO_2 reduction to CO with large currents, highlighting the excellent electrocatalytic activities of such layers, which combine porosity, electronic conductivity and synergetic properties from its components.

Keywords: Hybrid material, nanomaterials, molecular catalyst, cobalt complex, electrochemical CO_2 reduction

Introduction

Inorganic–organic hybrid materials are a class of compounds gaining more and more interest due to their distinct chemical and physical properties.[1] They are disordered physical-chemical systems in which inorganic components (metal ions, oxides, sulfides, non-metallic elements, etc.) and organic components (organic molecules, ligands, biomolecules, polymers, etc.) are brought together by specific interactions resulting in a synergistic enhancement of their functional properties,[2] opening up new fields of properties and functional capabilities that would not be possible with just one of the components. This growing field of research has found

a wide range of applications such as energy storage, high performance capacitors, solar cells, catalysis and photocatalysis.[3,4] Otherwise, electrocatalytic reactions such as reduction of CO_2 (CO_2RR) is an appealing option for storing renewable electricity and producing valuable chemicals and fuels such as CO, HCOOH, CH_4, CH_3OH, or CH_3CH_2OH,[5] in a sustainable manner. The reaction is not only a thermodynamically uphill process, but also suffers from slow kinetics. Moreover, poor catalytic selectivity and high overpotential continue to limit efficiency and upscaling of CO_2 electroreduction.[6] The search for increased activity, selectivity and stability of catalysts requires new systems. The combination of organic and inorganic hybrid nanostructured materials can play a significant role in this direction. While using nanostructured or high surface area catalysts can significantly improve surface reactivity by making a significant fraction of the reactive sites available for catalysis, the use of organic-inorganic hybrid materials can open up the possibility of addressing new properties of catalysts that would otherwise be inaccessible using purely organic or inorganic materials.

Currently, a variety of earth-abundant metal-based molecular catalysts have been identified reporting high selectivity for the CO_2 reduction reaction.[5,7–9] Among examples, cobalt phthalocyanine has been identified as good electrocatalyst for CO_2RR owing to its high selectivity and activity for CO production.[10,11] Besides, oxide-derived metal based materials such as CuO, Cu_2O,[12–15] Ag_2O,[16,17] NiO,[18,19] and TiO_2,[20,22] have been successfully demonstrated to be active and selective catalysts for CO_2 reduction. ZnO, a low toxic compound, is an oxide-derived non-noble metal with promising optical,[23] electronic,[24] photovoltaic,[25,27] and catalytic properties.[28–31] Recently a maximum faradaic efficiency (FE) of 92% for CO_2 to CO conversion has been reported for a nanoporous ZnO.[32] However, the catalytic system suffered from degradation issues due to morphological change during CO_2 reduction in aqueous media.

ZnO has the distinct advantage of being easily prepared in high quality and in a wide range of nanostructures, such as nanorods,[33,34] nanotubes,[35,36] nanobelts,[37,38] via solution routes such

as chemical bath deposition (CBD)/dip coating,[9] chemical vapor deposition (CVD)/spray pyrolysis,[40] hydrothermal synthesis,[41] and electrochemical deposition.[42,43]. Electrodeposition is low temperature (mostly <100°C) cost-effective deposition process that allows the design of complex ZnO nanostructures by combining and adjusting the growth conditions.[33,34,44,45] In the late 1990s, Yoshida and co-workers[46] described a one-step electrodeposition of nanostructured ZnO/organic films onto conducting substrates for photovoltaic applications, by adding water-soluble dyes such as tetrasulfonated metallophthalocyanines to the electrochemical bath containing $Zn(NO_3)_2$. The loading of organic molecules into ZnO films was also attempted using a $ZnCl_2$ bath employing cathodic reduction of dissolved molecular oxygen precursor.[47,48] In the present study, electrodeposited ZnO layer will be used as matrix for the incorporation of molecular catalysts.

Incorporation of molecular catalysts onto the surfaces of electrodes can be achieved in a variety of manners. Typically, grafting methods are used where the catalyst's ligand structure is chemically modified with appropriate anchoring groups that allows surface binding in either through a non-covalent or a covalent mode. Polymer binders can also be used to immobilize catalysts on the surface of electrodes.[49] However, immobilized catalyst on the electrodes surface must remain stable for long periods of time under catalytic operating conditions. In addition, immobilization should not hinder the catalytic activity of the complex. Developing nanostructure organic-inorganic hybrid catalysts in which a metal oxide can act as a porous cage that grows around the molecular catalyst, allowing the diffusion of substrate and product molecules in and out of the catalytic material, not only can prevent the catalyst from leaching out, but also can provide large electrochemical surface areas, and increases CO_2 adsorption capacity around the active sites, resulting in excellent efficiency and long-term stability in CO_2 reduction. However, to our knowledge, very limited reports have exclusively focused on implementing this strategy in the electrochemical reduction of CO_2.

Herein, we present the preparation of molecular metal complexes-modified nanostructured zinc oxide (ZnO) thin films electrodes, focusing in the attractive ability to tune their chemical, optical, electrical, and catalytic properties by altering the film composition and thickness. The strength of the proposed method lies in its one-step electrodeposition route to produce nanoporous or nanostructured oxide matrix while simultaneously encapsulating the catalyst. Two different nanostructured electrodes with self-supported catalyst hybrid layers were developed. First, **CoPcTA**, a water-soluble tetracationic Co phthalocyanine complex, was designed to act as an encapsulated molecular catalyst within a transparent and conductive ZnO nanoporous matrix. In a two-step deposition process, the aforementioned hybrid layers were also deposited on ZnO nanorods, resulting in 3D ZnO hierarchical structures (Figure 1). Finally, the possibility of replacing **CoPcTA** with other water-soluble molecular catalysts such as tetra-sulfonated cobalt phorphyrin (**CoTSPP)** or a tetra-sulfonated nickel phthalocyanine (**NiTSPc)** has been investigated, emphasizing the versatility of the preparation method, which could be used for the incorporation of a wide range of molecular complexes containing various metals and ligands. A combination of analytical, UV-vis, ICP, XPS, ATR-IR, and EDX-mapping techniques was used to confirm the incorporation and potential synergy between metal organic catalysts and the oxide matrix. Linear/cyclic voltammetry and controlled potential electrolysis (CPE) experiments confirmed the accessibility and catalytic activity of the hybrid organic-inorganic layers. Material characterization and redox behavior versus CO_2 reduction have been investigated, demonstrating homogeneous dispersion and control of molecular metal complex loading through the oxide matrix. These hybrid electrodes were tested as cathode material in electrocatalysis. Taking as illustrative example the CO_2 reduction, their remarkable potential was demonstrated.

Results and Discusssion

Hybrid electrodes' preparation and characterization. In this work, electrodeposited ZnO was first used as a matrix for incorporation of **CoPcTA**, a water-soluble molecular Cobalt phthalocyanine catalyst. A glass covered with 350 nm of ZnO:Al layer deposited by atomic layer deposition (ALD) was used as substrate. The procedure to fabricate the nanostructured electrodes is schematically shown in Figure 1, along with microscopic characterization data (Figure 2). Two nanostructured layers have been developed and combined with a molecular catalyst: nanoporous **ZnO|CoPcTA** structure (NP) (Figure 1a) and 3D hierarchical structure made of 20 nm of nanoporous **ZnO|CoPcTA** structure (NP) grown on zinc oxide nanorods (ZNRs) (Figure 1b).

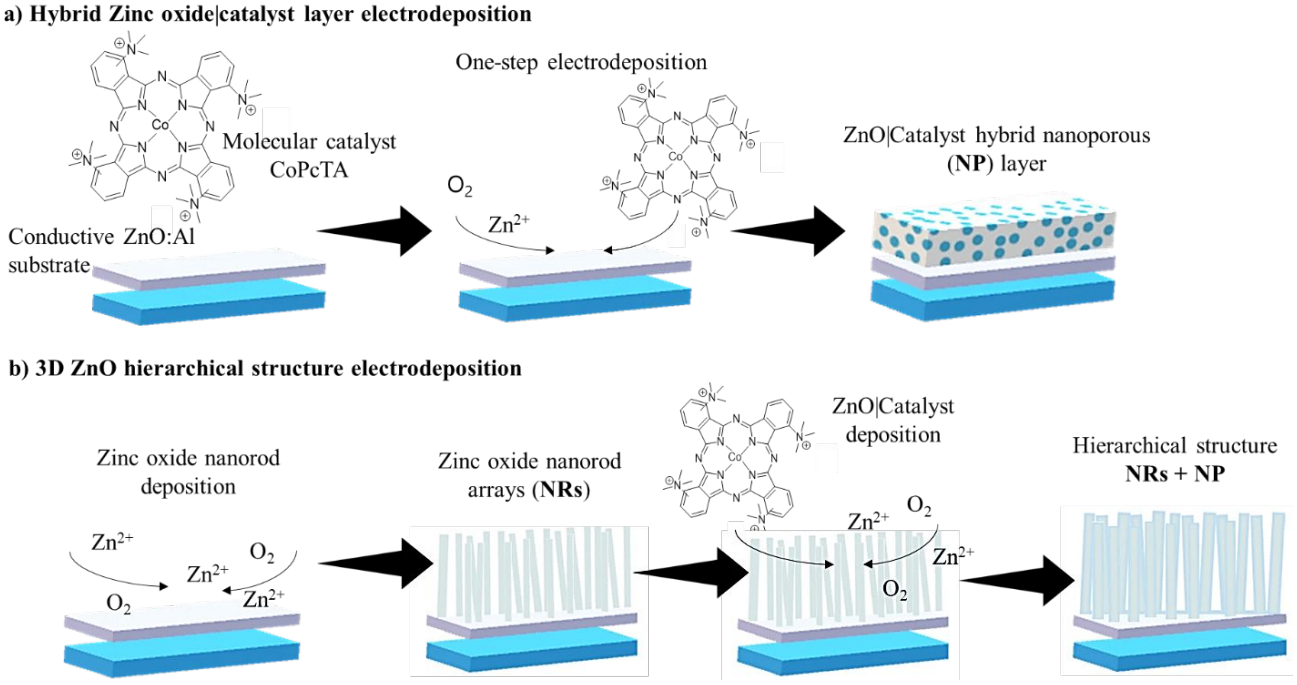

Figure 1 Schematic representation of the preparation of the ZnO nanostructures. a) Hybrid **ZnO|CoPcTA** nanoporous (**NP**) layers, b) Hierarchical 3D structures made of zinc oxide nanorod arrays (**NRs**) coated by a hybrid ZnO|catalyst nanoporous (**NP**) layer (**ZnO NRs + ZnO|CoPcTA NP**).

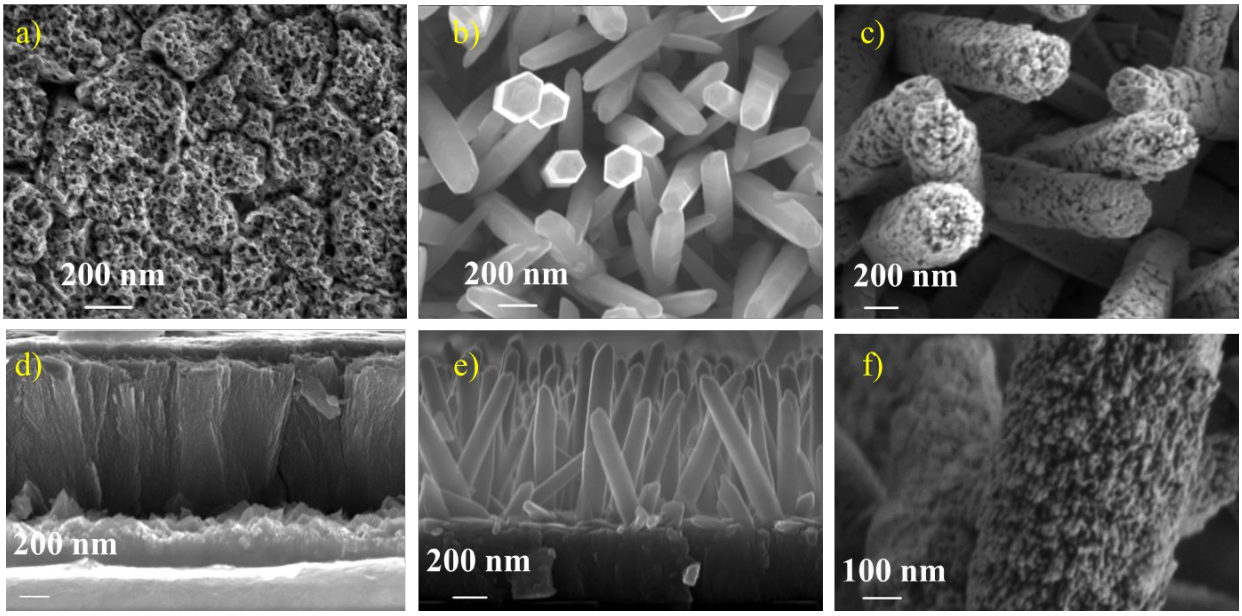

Figure 2 Top view and cross section SEM images of the different ZnO nanostructures presented in this work: a,d) **ZnO|CoPcTA NP**, b,e) **ZnO NRs**, c,f) **ZnO NRs** covered by a thin **ZnO|CoPcTA NP** layer.

The electrodeposition of the **ZnO|CoPcTA** hybrid layers was carried out at constant potential in an aqueous oxygen saturated solution containing $ZnCl_2$, KCl salts and **CoPcTA** (see experimental section for details). Figure 3 compared the X-ray diffraction patterns under grazing incidence (GIXRD) of the ALD-ZnO:Al substrate with those of a **ZnO|CoPcTA NP** layer, pure **ZnO NRs**, and a hybrid 3D structure of **ZnO NRs** covered by a ~20 nm **ZnO|CoPcTA NP** layer. For all layers, the diffraction patterns match the standard diffraction patterns of the hexagonal wurtzite ZnO crystal structure (JCPDS-36-1451).[50] ALD ZnO:Al substrate (Figure 3a) presents a mixed (100), (101) and (110) orientation indicating that the c-axis of ZnO is mostly parallel to the substrate. As observed on the SEM images (Figures 2a & 2d), addition of the molecular catalyst during the growth of ZnO seems to strongly affect the crystal growth mechanism of the ZnO, leading to a significantly higher surface area, resulting in a sponge like nanoporous structure. The comparison of the X-ray diffraction patterns of **ZnO|CoPcTA** nanoporous layer with the ALD ZnO:Al substrate show an increased peak intensity of the (002) planes for the nanoporous layer as well as appearance of (102) and (103) reflections (Figure

3c). The nanoporous film is thus mainly oriented according to the (002) reflection which corresponds to the c-axis of the wurtzite type lattice. Such preferential orientation is often observed for ZnO layers, as the (002) crystal face is the densest and the most stable thermodynamically.

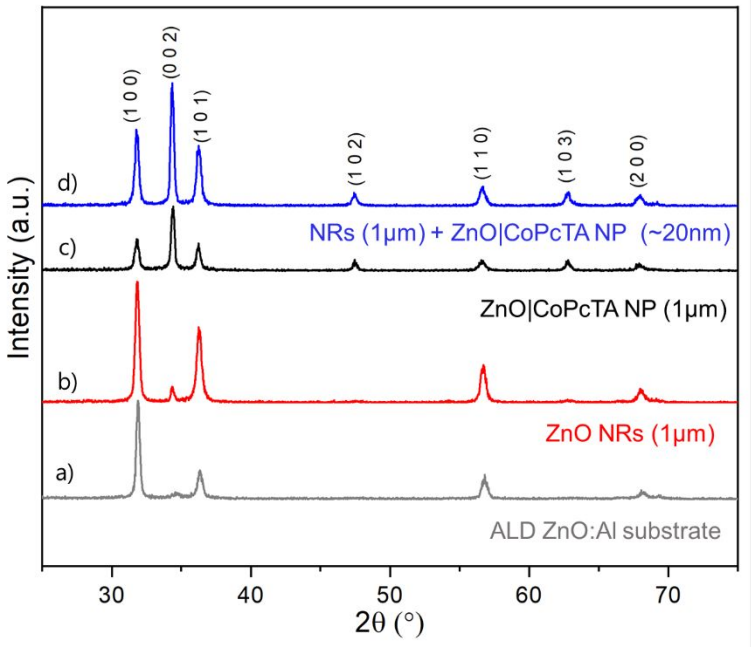

Figure 3 GIXRD patterns under grazing incidence for: a) ALD ZnO:Al substrate, b) **ZnO NRs** 1 µm grown on ALD ZnO:Al substrate, c) **ZnO|CoPcTA NP** layer grown on ALD ZnO:Al substrate and d) **ZnO NRs** covered by **ZnO|CoPcTA NP** layer (NRs + NP).

When **ZnO NRs** are grown on ALD ZnO:Al substrate, it results in non-vertical randomly oriented rods as observed on SEM images (Figures 2b and 2e), while presenting the same crystalline orientation and diffraction plans as the ALD-ZnO:Al substrate (Figure 3b). Interestingly when **ZnO|CoPcTA NP** layer is grown on **ZnO NRs** (Figure 3d), the same preference orientation occurs as with the **ZnO|CoPcTA NP** layer for which the most intense peak remains the (002). This confirms that, when **CoPcTA** is added to the deposition bath, whatever the substrate orientation, nanoporous layers tend to self-organize with a preferential c-axis orientation along (002) plane. For these layers, SEM pictures show a hierarchical structure composed by a hybrid **ZnO|CoPcTA NP** coat surrounding the nanorods (Figures 2c and 2f).

Effective covering of **ZnO NRs** arrays with **NP** layers has been achieved by varying the total charge transferred during the electrodeposition (Supplementary Figure S1).

The thickness of the **ZnO|CoPcTA NP** layer can be controlled by varying the transferred charge throughout the process. Increasing the charge from 0.5 to 4 C cm^{-2} results in a linear increase in NP layer thickness from 20 nm to 1200 nm (Supplementary Figure S2). It has been shown that, adding a water-soluble molecular complex to the ZnO electrodeposition bath can not only act as a structure directing agent but also results in its incorporation inside the nanoporous ZnO layer.[44,47] Inductively coupled plasma optical emission spectrometry (ICP–OES) and optical absorption measurements on **ZnO|CoPcTA NP** samples were performed to confirm the incorporation of the molecular catalyst into the electrodeposited layers (Supplementary Figure S3). The results of ICP measurements are presented in Figure 4b, showing that after dissolution of the layers (acidic treatment with water diluted nitric acid), catalyst loadings ranged from 0.8 ± 0.2 nmol cm^{-2} for a **ZnO|CoPcTA NP** layer 50 nm thick, up to 7.8 ± 0.7 nmol cm^{-2} for **ZnO|CoPcTA NP layer** 1 μm thick. The concentration of the **CoPcTA** molecule in the layers is linearly correlated to the film thickness. Furthermore, the optical absorbance measurements show that the **ZnO|CoPcTA NP** samples present an absorbance peak, around 665 nm, in a wavelength range which is close to the absorbance peak of **CoPcTA** molecule in aqueous solution (Figure 4a). A linear relationship is observed between layer thickness and the **CoPcTA** concentration inside the layer (Supplementary Figure S4), as well as between the layer thickness and the absorbance at 665 nm (Figure 4b). This strongly suggests the molecule's incorporation into the hybrid layers, the amounts of which can be adjusted by controlling the deposition time (i.e. the charge transferred).

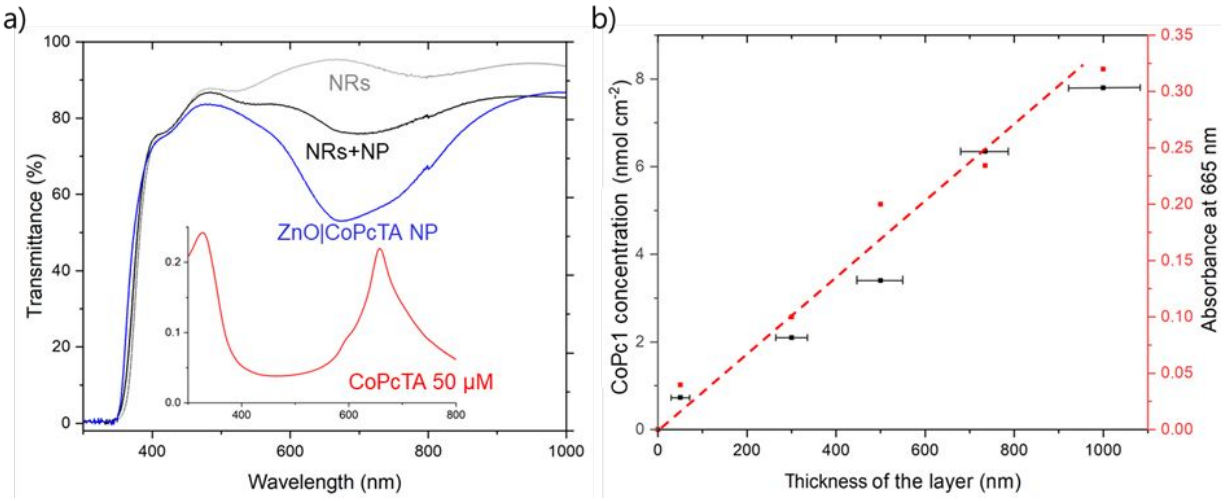

Figure 4 a) Optical transmission of electrodeposited **ZnO NRs** (1 µm, grey), **ZnO|CoPcTA NP** layer (1 µm, blue) and 3D ZnO **NRs** (1 µm) coated by a **ZnO|CoPcTA NP** (20 nm, black), on ALD-ZnO:Al. Inset: Absorbance of the **CoPcTA** molecule in aqueous solution (concentration = 50 µM, red). b) Concentration of **CoPcTA** molecules in the **ZnO NP** layers measured by ICP as a function of the thickness of the layer and comparison to the absorbance of the same samples at λ = 665 nm.

The incorporation of molecular catalysis in **ZnO|CoPcTA NP** being confirmed, ICP analysis were performed on a 3D **ZnO NRs** (1 µm) covered with 20 nm of **ZnO|CoPcTA NP** layer. In these layers, the ICP analysis shows a **CoPcTA** concentration around 0.73 nmol cm^{-2}, which corresponds to approximately ten times less than the one measured for a 1 µm thick **ZnO|CoPcTA NP** layer.

Figure 3a compared optical transmission of electrodeposited **ZnO NRs** (1 µm), **ZnO|CoPcTA NP** layer (1 µm) and 3D **ZnO NRs** (1 µm) coated by a **ZnO|CoPcTA NP** (20 nm), on ALD-ZnO:Al substrate and the absorbance of an aqueous solution of the pure **CoPcTA** molecule (50 µM). In the visible range, the transparency of **ZnO NRs** approaches 90%. The impact on the total transmission of the incorporation of the **CoPcTA** molecule into the nanoporous **ZnO|CoPcTA NP** layers becomes clear between 525 and 1000 nm, with a decrease from ~97% transmission to ~55% (580 to 700 nm range) for a 1 µm thick **ZnO|CoPcTA NP** layer. Such

decrease originates from Co complex incorporation, **CoPcTA** presenting an absorption peak around 665 nm. Optical transmission is significantly improved (>75%) upon using hierarchical structure **ZnO NRs+NP** thanks to the very low amount of catalyst incorporated in the structure.

Dispersion and distribution of the catalyst into the nanoporous layers was also investigated by EDX-mapping measurement. Images from a 1 µm thick **ZnO|CoPcTA NP** electrode (Supplementary Figure S5) show signals from the O, Zn, Cl atoms of the ZnO matrix, but also signals from Co, definitively confirming the catalyst incorporation into the film during the electrodeposition. Additionally, mapping of Co element revealed the absence of cobalt aggregates, suggesting a homogeneous distribution of the catalyst in the oxide material.

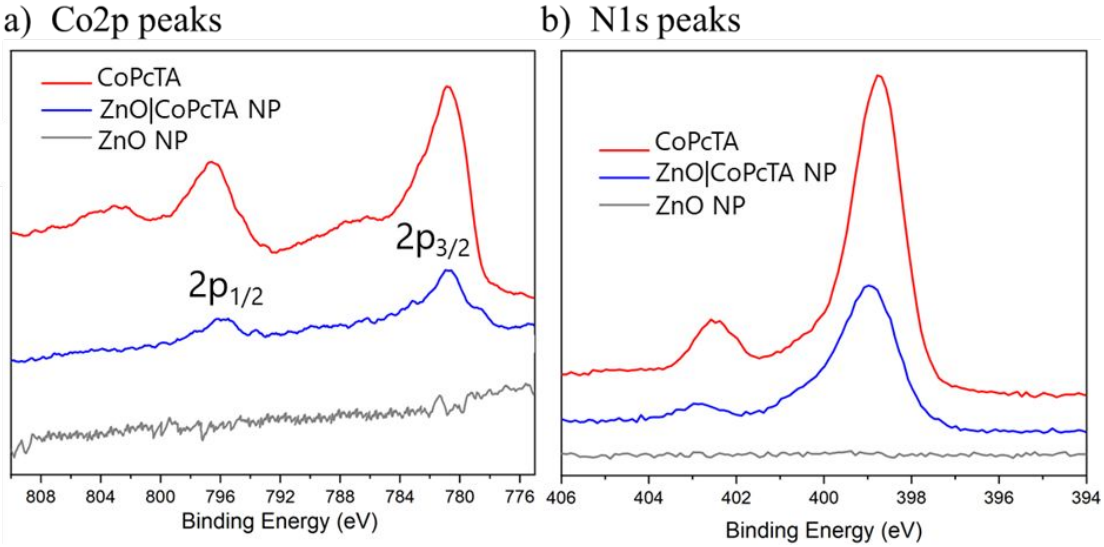

Figure 5 Comparison of the XPS core level spectra of (a) Co 2p, (b) N 1s for: **CoPcTA** molecule, **ZnO|CoPcTA NP** electrode and a blank ZnO electrode.

XPS measurements were performed to assess the presence of the **CoPcTA** molecule and its eventual interaction with the electrodeposited ZnO matrix. The Co 2p and N 1s signals obtained for **CoPcTA**, **ZnO|CoPcTA NP**, and a blank ZnO layer with no molecular complex are compared in Figure 5. From **ZnO|CoPcTA NP**, two peaks corresponding to Co 2p signals indicative of a Co^{2+} oxidation state are observed (Figure 5a), with a main peak ($2p_{3/2}$) at 780 eV

and a secondary peak at ($2p_{1/2}$) at 796 eV.[51] In Figure 5b, signals from nitrogen were also detected on the surface of the **ZnO|CoPcTA NP** electrodes, with N1s signal peak at 398.8 eV, a similar value to the characteristic binding energy of the isoindolic N in phthalocyanines complexing a cobalt atom (BE = 399.3 eV).[51] This peak reflects the configuration of the CoN_4 centre with four equivalent nitrogen atoms coordinating a Co^{2+} ion. Furthermore, a small additional N1s peak centred at 402.5 eV is observed, which is typically assigned to N–O bonds,[52] indicative of a possible interaction between the N atoms of the **CoPcTA** molecule and of the oxygen atoms of the sample holder (Si wafer covered by native oxide). All these results clearly confirm that **CoPcTA** is incorporated into the hybrid **ZnO|CoPcTA NP** layer. In order to have a better understanding of the interactions between the molecular catalyst and the inorganic ZnO matrix, the O 1s and Zn 2p XPS spectra of **ZnO|CoPcTA NP** layers were also compared to the blank ZnO layers (Supplementary Figure S6). Observed peaks do not show any shift in the binding energy value before and after the incorporation of the molecular catalyst. However, further analysis must be done in the future to probe for the possible interactions between the molecule and the ZnO inorganic matrix.

The infrared spectroscopy analysis (ATR-IR) of **CoPcTA**, of a 1 µm **ZnO|CoPcTA NP** sample and of a ZnO blank sample were also compared (Supplementary Figures S7). The analysis data revealed similar fingerprint regions between **CoPcTA** powder and **CoPcTA** loaded into the **ZnO|CoPcTA NP** layer, which further evidences that the catalyst is well entrapped into the ZnO electrodeposited layer. The metal to ligand (M–N) vibration of **CoPcTA** could be observed at 910 cm^{-1}, as well as peaks around 1080 cm^{-1} (C–N stretching bending vibrations) and at 1393 cm^{-1}. These latter are assigned to aromatic ring stretching vibrations, showing a perfect match with the vibration obtained with a **CoPcTA** powder sample. The peaks from the CH_3 groups at 2895 and 2986 cm^{-1} indicate structural preservation of the organic molecule upon incorporation into the ZnO inorganic matrix.[53]

Electrochemical CO_2 reduction by ZnO|catalyst hybrid nanostructures. The catalytic activity of the **ZnO|CoPcTA NP** electrodes was first explored by cyclic voltammetry (CV) in an acetonitrile solution containing 0.6 M H_2O and 0.1 M tetrabutylammonium hexafluorophosphate ($TBAPF_6$). A catalytic current with an onset potential at ca. -1.6 V vs. SCE was observed when the solution was saturated with CO_2 (Figure 6a). Addition of H_2O as proton source (0.33 M, 0.44 M and 0.67 M respectively) was investigated. As observed in the cyclic voltammograms (Supplementary Figure S8a), H_2O concentration increase resulted in an enhancement of the current density and in a decrease of the overpotential of ca. 200 mV upon going from 0.33 to 0.67 M H_2O. Adding more water (> 0.7 M) did not show a significant impact on the current density, but accelerated the degradation of the electrodes. Furthermore, increasing the thickness of the NP layers allows to reach higher current densities, as quantified by CVs of 50 nm, 530 and 1000 nm thick **ZnO|CoPcTA NP** layers that displayed c.a. 0.5, 1.4 and 2.0 mA cm^{-2} respectively (Supplementary Figure S8b). The increase of the current density with the thickness of the NP layer suggests that the current density depends on the active surface area of the electrodes as well as the amount of catalyst inserted into the layers. Thanks to the nanoporous structure of the electrodes, the reactant CO_2 can access to the active sites even in a 1 μm thick layer.

This was confirmed upon performing CPE experiments. A comparison of electrodes covered with a **ZnO|CoPcTA NP** layers of 50 ± 10 nm, 530 ± 50 nm and 1000 ± 70 nm thickness respectively (Supplementary Figure S9) showed current density increase with the thickness of the **NP** layer. Even with 1 μm thick layer, the **CoPcTA** molecules incorporated into the ZnO nanoporous matrix are accessible and can react with CO_2, the electrocalalytic overall process is only partially limited by diffusion of the reactant and charge transport through the oxide film. Moreover, these results add further evidence that the **CoPcTA** catalyst is well dispersed and distributed throughout the thickness of the layer and not just on the surface. The electrodes showed a good stability for 45 minutes CPE. During the first 10 minutes, the current gradually

increased until it reached a steady-state value staying stable until the end of the experiment. This behavior may be due to the porosity of our layers, since it takes some time for the reactant (CO_2) to fill and reach all the porosity of the layer; in addition, similar time effect may also impact the progressive charging of the film (charge transport to the catalytic sites).

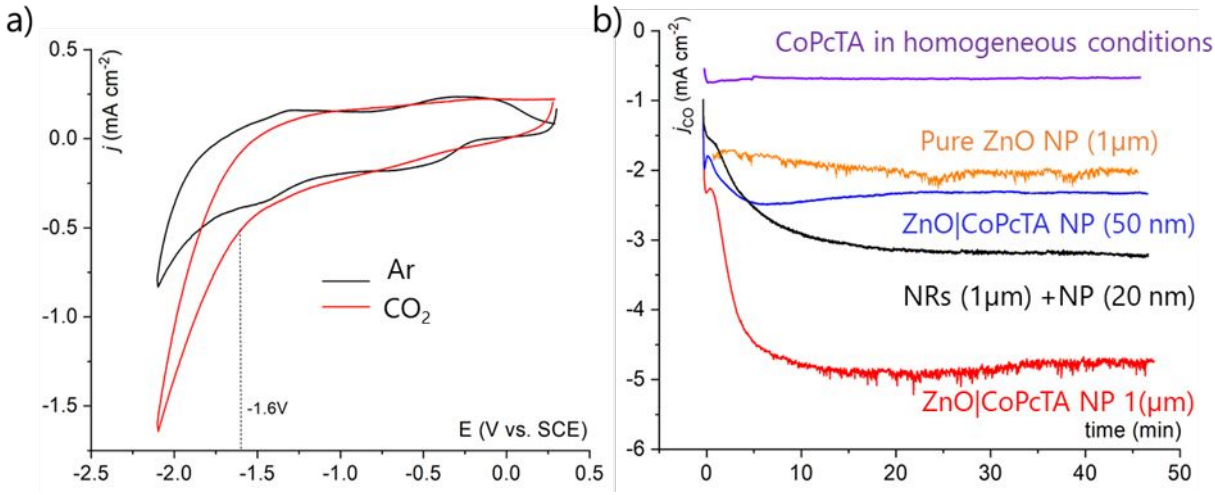

Figure 6 (a) Cyclic voltammograms recorded in Ar (black) and CO_2 (red) saturated acetonitrile solution + 0.1 M $TBAPF_6$ at a 1 µm thick **ZnO|CoPcTA NP** electrode. Electrode surface 0.5 cm^2, scan rate 0.1 V s^{-1}. (b) CPE at E = -2.1 V vs. SCE in a CO_2 saturated acetonitrile solution + 0.1 M $TBAPF_6$ and 0.67 M H_2O for: **CoPcTA** (0.5 mM) in homogeneous conditions (purple), a 1 µm thick ZnO porous layer without catalyst (orange), a 50 ± 10 nm thick **ZnO|CoPcTA NP** layer (blue), a 1 µm thick **ZnO NRs** covered by a 20 nm thick **ZnO|CoPcTA NP** (**NRs+NP**) layer (black) and a 1000 ± 70 nm thick **ZnO|CoPcTA NP** layer (red).

CPE experiments at E = -2.1 V vs. SCE (45 min duration) were performed with all electrode structures and are compared in Figure 6b. First, the **CoPcTA** molecule in homogeneous conditions showed a weak catalytic activity with a current density of -0.45 mA cm^{-2}, while gas chromatography (GC) analysis of the products indicated formation of CO with 60.8 % selectivity (Table 1, entry 1). A ZnO nanoporous layer can reduce CO_2 to CO with 73.7 % selectivity at j = -2 mA cm^{-2} (Table 1, entry 2), i.e. a partial current density for CO production j_{CO} = -1.5 mA cm^{-2}, confirming catalytic activity of the ZnO itself to reduce CO_2 to CO, as reported previously.[29,32,53–58] When both components, **CoPcTA** complex and ZnO are

combined in a hybrid material, significant enhancement of the CO_2 reduction reaction is obtained. CPE experiments using **ZnO|CoPcTA NP** layers led to typical current density ranging from -2.45 mA cm^{-2} up to -5 mA cm^{-2} (i.e. ranging from j_{CO} = 2.4 mA cm^{-2} to j_{CO} = 4.95 mA cm^{-2} respectively), when layer thickness increases from 50 to 1000 nm respectively, while producing CO with selectivity above 97 % (Table 1, entries 3-5). The presence of a small amount of **CoPcTA** into the layers induces not only an important increase of the current density but also strongly improves the selectivity of the reaction. These results illustrate the synergetic effect of the cobalt complexes and zinc oxide for boosting the catalysis, possibly occurring from the joint coordination of CO_2 molecules at the cobalt sites along with assistance from the zinc ions (Lewis acid sites) which provide stabilisation of the partial negative charge developing on the oxygen atoms of the CO_2 and weakening of the C-O bonds. Remarkably, turnover number (TON) as high a 17,885 and turnover frequency (TOF) of 9.4 s^{-1} were obtained for the thin (50 nm) NP layer (Table 1, entry 3), standing among the highest performance so far obtained for an immobilised metal complex electrocatalyst.[6,10,59] TOF value decrease slightly when the thickness of the layer increases (Table 1, compare entries 3, 4 and 5), meaning that an overall faster catalysis occurs in a thin layer compare with a thick layer, which may be due to progressive growing influence of charge transport and diffusional effect limitation in the thicker layers, even if the current density increases across the series of electrodes.

Comparison of CPE experiments of an electrode with a 50 nm **ZnO|CoPcTA NP** thin layer (Figure 6b, blue) with a 3D nanostructured electrode (**NRs** 1µm covered by a **ZnO|CoPcTA NP** 20 nm, Figure 6b, black line), both incorporating a similar amount of molecular catalyst (0.85 nmol cm^{-2} and 0.73 nmol cm^{-2} respectively), showed an enhancement of the catalytic performance towards the CO_2RR for the 3D structure. The partial current density j_{CO} reached by the NP thin layer for CO production is ca. -2.4 mA cm^{-2} whereas the 3D structured electrode achieved an absolute higher (j_{CO} = -2.8 mA cm^{-2}) current density. The 3D structured electrode

also furnished a higher TOF of 11.7 s^{-1} (Table 1, compare entries 3 and 7), meaning that the CO production goes fast in the 3D nanostructured electrodes. Combination of good electronic transport properties and the high exposed surface of the **ZnO NRs** with the catalytic hybrid layer results in an enhancement of the catalytic performance towards the CO_2RR.

Table 1. Comparative data of performance of the different ZnO nanostructures catalytic materials during a 45 minute electrolysis experiment at a constant potential E = -2.1 V vs. SCE in CO_2-saturated acetonitrile solution containing 0.1 M $TBAPF_6$ and 0.67 M H_2O. Electrode surface = 1 cm^2.

Entry	Sample	Catalyst amount	Current density (mA cm^{-2})	Total FE (%)	Selectivity %CO	Selectivity %H2	TON	TOF (s^{-1})
1	**CoPcTA** in homogeneous solution	0.5 mM	-0.45	98.1	60.8	39.2	0.93	0.001
2	Blank ZnO nanoporous layer 1000 nm	0	-2.04	99.0	73.7	26.3	-	-
3	**ZnO|CoPcTA NP** 50 ± 10 nm	0.81 nmol	-2.45	98.6	97.4	2.6	17885	9.4
4	**ZnO|CoPcTA NP** 500 ± 50 nm	1.86 nmol	-3.37	99.6	98.4	1.6	9283	4.9
5	**ZnO|CoPcTA NP** 1000 ± 70 nm	2.80 nmol	-5.0	97.1	98.9	1.1	8280	4.4
6	ZnO **NRs** 1µm	0	0.9	98.0	73.5	26.5	-	-
7	ZnO **NRs** 1µm + **ZnO|CoPcTA NP** 20 nm	0.75 nmol	-2.9	91.0	96.7	3.3	22242	11.7

We investigated the stability of the electrodes upon performing long-term CPE at −2.1 V vs. SCE (2 h) using two samples **ZnO|CoPcTA NP** layers 750 ± 50 nm thick (Figure 7). Average catalytic current of 3.5 mA cm^{-2} were obtained. Gas chromatography analysis of the products indicated the formation of CO with ca. 97% FE along with H_2 as only by-product (3%), giving a complete Faradaic efficiency. The current density, after reaching a steady-state value in the first 5 min, remained stable along the electrolysis with only a slight decay. ICP analysis of the electrode before and after 2 h of electrolysis revealed a 10% loss of the catalyst from the electrode to the solution. This decrease may reflect partial cathodic reduction of the ZnO into metallic Zn, which could further lead to some catalyst leak. To verify this hypothesis, XPS analyses were performed to characterize the surface properties of the samples before and after

CPE. Due to the comparable binding energies of Zn and ZnO in the Zn 2p region of the XPS spectrum, we compared the Zn LMM Auger peaks of the as-prepared and used **ZnO|CoPcTA NP** samples. As shown in Fig S10a, both samples exhibited the typical Auger peaks of ZnO, with a main peak at ~499 eV and a shoulder at ~496 eV. Notably, no Zn peaks are present after CPE. However, XRD measurements of the **ZnO|CoPcTA NP** sample after CPE (figure S10b) showed the presence of diffraction peaks from Zn at 2θ = 43.1° and 54.2° corresponding to the (101) and (102) lattice planes of hexagonal phase from Zn metal respectively,[60] indicating that a fraction of the oxidized Zn species were reduced to metallic Zn during electrolysis. Part of the layer may thus have been dissolved which could explain the loss of the catalyst. Overall, the above results indicate that the **ZnO|Catalyst** films are quite stable with catalytic activity being sustained for hours.

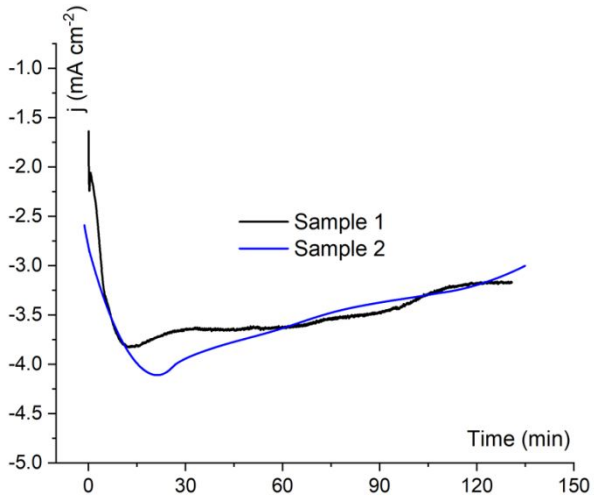

Figure 7 CPE at E = -2.1 V vs. SCE in a CO_2 saturated acetonitrile solution + 0.1 M $TBAPF_6$ and 0.67 M H_2O for two 750 ± 50 nm **ZnO|CoPcTA NP** layer electrodes.

In addition to the **ZnO|CoPcTA NP** layers, a porphyrin Cobalt complex (**CoTSPP**) and a Nickel phthalocyanine complex (**NiTSPc**), both bearing four sulphonated groups, were used to grow ZnO nanoporous layers **ZnO|CoTSPP NP** and **ZnO|NiTSPc NP**. CPE experiments were performed with these electrodes of similar thickness and compared with those investigated

before. Total current density of -1.85, -1.75 and -1.7 mA cm^{-2} were respectively obtained for **ZnO|CoPcTA NP**, **ZnO|CoTSPP** and **ZnO|NiTSPc NP** electrodes (Supplementary Figure S11). They showed very similar selectivity for CO production, 93.3%, 96.9%, and 96.8% respectively (Supplementary Table S1).

The electroreduction of CO_2 exemplified in the above described examples illustrate the versatility of the preparation method that could be used for the incorporation of a variety of molecular complexes with different metal and ligands with a systematic positive impact of the metal oxide matrix, thus opening a wide range of possibilities for performing various electrocatalytic reactions.

Conclusions

Hybrid ZnO|catalyst films have been electrodeposited on transparent conductive electrodes by a simple one-step method. The grown nanostructured oxide layers are highly porous and can be loaded with water soluble metal (e.g Co, Ni) complexes during the electrodeposition process. Both the thickness (from a few tens of nm to a μm) and nanostructuration (2D, 3D hierarchical structures) of the oxide layers can be controlled, as well as the quantity of encapsulated molecular complexes, which appear to be homogeneously dispersed in the films. These films are electrochemically active thanks to high porosity and conductivity. Such modified electrodes may be used for various applications in electrochemical devices. As an illustrative example, selective and fast electroreduction of CO_2 to CO has been achieved, showing synergetic effect between the molecular catalyst and the zinc oxide hosting matrix. Such approach could now be applied to other electrocatalytic processes. Remarkably, these electrodes also present a significant visible light transmission, which may enable their use as a front contact in photovoltaics and photocatalytic devices. This opens up for a modular approach where the photo-absorber and the molecular-catalysts can be developed, tested, optimized, and exchanged independently.

Methods

Catalyst synthesis. Reagents were purchased from Aldrich and used without further purification. 3-(dimethylamino)phthalonitrile was synthesized according to literature.[10] (See catalyst synthesis characterizations in Supplementary). Tetra-sulfonated cobalt porphyrin **CoTSPP** and tetra-sulfonated nickel phthalocyanine **NiTSPc** were purchased from Aldrich.

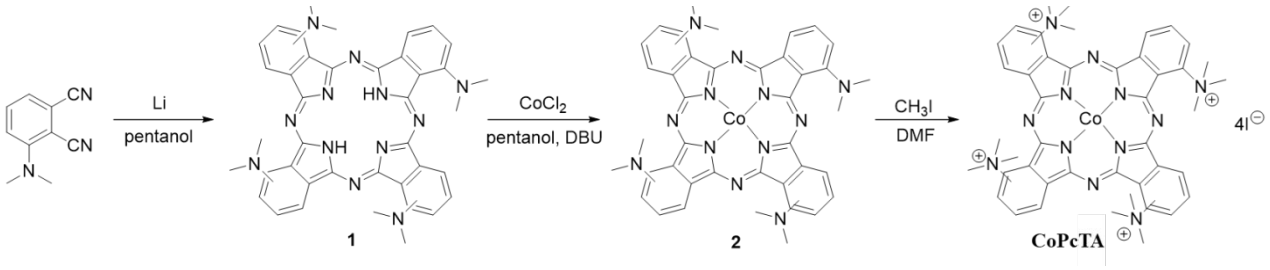

Figure 8. Synthetic route for CoPcTA

Synthesis of phthalocyanine **1**. Granules of lithium were added to anhydrous n-pentanol (10 mL). This mixture was heated to 60 °C under argon flux until total consumption of the granules. 3-(dimethylamino)phthalonitrile (0.5 g, 2.92 mmol) was added and this reaction mixture was refluxed for 18 h. It was then cooled to room temperature and poured into an ethanol/water mixture. The resulting precipitate was filtered off, washed several times with water and dried. Phthalocyanine **1** (Figure 8) was obtained by chromatography on silica gel using a mixture of CH_2Cl_2/EtOH (20:1) as the eluent. Yield: 35% (175 mg). FT-IR (ν, cm^{-1}): 3290, 3073, 2944, 2832, 2775, 1576, 1485, 1433, 1321, 1186, 1135, 1083, 1035, 970, 879, 804, 745, 667. ^{1}H NMR (500 MHz, DMSO-d_6): δ, ppm, 3.64 (m, 24H), 7.45-8.10 (m, 8H), 8.87 (m, 4H). ESI-HRMS: m/z 687.33840 $[M]^+$ calculated for $C_{40}H_{38}N_{12}$: 686.8280. UV-vis (DMSO): λ_{max} nm (log ε) 342 (4.70), 712 (4.78), 779 (4.89).

Synthesis of phthalocyanine **2**. Phthalocyanine **1** (165 mg, 0.24 mmol), $CoCl_2$ (72 mg, 0.48 mmol), and DBU (1 mL) in dried n-pentanol (10 mL) was heated to reflux for 18 h under argon.

After cooling to room temperature, the reaction mixture was poured into an ethanol/water mixture. The resulting precipitate was filtered off and washed several times with water. Phthalocyanine **2** was purified by chromatography on silica gel using a mixture of CH_2Cl_2/EtOH (10:1) as the eluent. Yield: 70% (125 mg). FT-IR (ν, cm^{-1}): 3069, 2926, 2827, 2775, 1571, 1490, 1438, 1316, 1186, 1156, 1126, 1091, 1052, 987, 914, 870, 805, 740. ESI-HRMS: m/z 744.2588 $[M]^+$ calculated for $C_{40}H_{36}CoN_{12}$: 743.7452. UV-vis (DMSO): λ_{max} nm (log ε) 331 (4.57), 733 (4.68).

Synthesis of phthalocyanine **CoPcTA**. Phthalocyanine **2** (150 mg, 0.20 mmol) was dissolved in DMF (10 mL), and methyl iodide (0.9 mL, 15 mmol) was added. The mixture was stirred at 45 °C for 16 h then poured into diethyl ether (25 mL). The resulting precipitate was filtered off, washed with ether and hexane. Yield: 90% (145 mg). FT-IR (ν, cm^{-1}) 3056, 3013, 2952, 2874, 2835, 2784, 1610, 1519, 1481, 1399, 1316, 1270, 1117, 996, 944, 805, 745. ESI-HRMS: m/z 804.3805 $[M+H]^+$ calculated for $C_{44}H_{48}CoN_{12}$: 803.8852. UV-vis (DMSO): λ_{max} nm (log ε) 330 (4.20), 702 (4.23).

Caution/important note: in order to destroy the excess of methyl iodide, the ether filtrate is treated with triethylamine.

Substrate preparation. Glass substrates (2 mm thick) covered by a transparent conductive zinc oxide aluminum doped (ZnO:Al) layer of 380 nm thick were used as working electrode for all the depositions. This ZnO:Al layer was deposited by Atomic Layer Deposition (ALD) according to reported procedure (sheet resistance from 20.1 to 28.2 × 10^{-3} Ω/sq).[61] The ZnO:Al coated glass substrates were ultrasonically sequentially cleaned in acetone, 2-propanol, and water, each for 5 min. They were activated in a KOH solution (pH 10.5) for 2 min and finally rinsed with distilled water prior to electrodeposition.

Preparation of the hybrid nanoporous catalytic layers (**ZnO|cat NP**). All oxide layers were electrodeposited using a classical three electrodes setup. The reference electrode was a saturated calomel electrode (SCE) (Hach) with a potential of +0.244 V vs. NHE at 25 °C. The counter electrode was a platinum wire and the working electrodes were the mentioned ZnO:Al coated glass substrates. The electrodeposition of the zinc oxide|catalyst nanoporous hybrid layers was carried out at constant potential E = -1.0 V vs SCE in an aqueous solution containing 5.0 mM $ZnCl_2$ (Sigma Aldrich >99.9%), 0.1 M KCl (ACS Reagent 99.0 – 100%) and 50 μM of the water-soluble catalyst (Cobalt phthalocyanine **CoPcTA**, tetra-sulfonated cobalt porphyrin **CoTSPP** or tetra-sulfonated nickel phthalocyanine **NiTSPc**). Oxygen gas was bubbled for 20 min prior to the deposition and the same gas flow was maintained during the whole deposition processes. Temperature was maintained at 70 °C. The thickness of the layers was controlled from few tens of nm to a micrometer by varying the transferred charge. The deposited films were rinsed with water, dried in air at 100 °C for 30 min, then stored at room temperature.

Preparation of the 3D hierarchical catalytic structures (**ZnO NR + ZnO|cat NP**). ZnO nanowire films were first prepared by electrodeposition on a ALD-ZnO:Al substrate, according to a method reported elsewhere.[33,34] The ZnO nanowire array layer was grown at 80 °C from a 0.2 mM $ZnCl_2$ and 0.1 M KCl solution saturated with O_2 by bubbling. (**ZnO NR**). The deposition process was stopped when the total transferred charge was 10 C cm^{-2}. The deposited films were rinsed with water and dried in air at 100 °C. These electrodes were then used for the deposition of the metal oxide|catalyst hybrid layers performed as described above, leading to a structure composed of zinc oxide nanorods surrounded by a nanoporous metal oxide/catalyst layer.

Electrochemical experiments. Cyclic voltammetry measurements (CVs) and Controlled potential electrolysis (CPE) were performed using a PARSTAT 4000A potentiostat (Princeton

Applied Research). The electrolyte was an acetonitrile solution with 0.1 M tetrabutylammonium hexafluorophosphate ($TBAPF_6$) (98%, Aldrich), and it was saturated with argon or CO_2 depending on the experiment. Electrodes with hybrid catalytic layers were connected with a clip protected by PTFE tape, and the electrical contact was ensured by using Gallium–Indium eutectic (Sigma Aldrich > 99.9%) covered with a copper tape. Copper was isolated from the electrolyte by the PTFE tape leaving an expose surface of 0.5 cm^2. The mentioned before reference electrode (SCE) was immersed in the same electrolyte in a separated compartment and positioned as close as possible from the working electrode. The counter electrode (platinum wire or mesh) is immersed in the same electrolyte but separated by a glass frit bridge.

The gases used were bought from Air Liquide. Electrolysis using CO_2 as the substrate were performed under 1 atmosphere of the gas, resulting in a concentration 314 ± 6 mM at 25°C.[62] The electrolysis experiments are performed in a sealed cell.

Products analysis. Gas chromatography analyses of the gases produced during electrolysis were performed with an Agilent Technologies 7820A GC system equipped with a thermal conductivity detector (TCD). CO and H_2 production were quantitatively detected and separated with a CP-CarboPlot P7 capillary column (27.46 m in length and 25 µm internal diameter). Temperature was held to 150 °C for the detector and 34 °C for the oven. The carrier gas was argon flowing at 9.5 $mL.min^{-1}$ at a constant pressure of 0.5 bar. The injections were performed with a 250 µL gas-tight (Hamilton) syringe. These conditions allow simultaneous detection of both H_2, O_2, N_2, CO, CO_2 and CH_4. Calibration curves were determined separately by injecting known quantities of pure gas. From product quantification TON and TOF were calculated using eqs. 1 and 2 respectively.

$$\mathrm{TON} = \frac{n_{product}}{n_{catalyst\ in\ the\ film}} \qquad (1)$$

$$\text{TOF} = \frac{TON}{t} \qquad (2)$$

Since the electrolysis experiments shown are not conducted until total deactivation of the catalyst, the given TON value can only be regarded as a lower estimation of the actual value. The amount of electrochemically active molecular catalyst can be an order of magnitude smaller than the amount of catalyst present at the electrode. It may also lead to an underestimated value of the calculated TON.[63] Calculations of TON and TOF are made considering the total amount of molecular catalyst added into the catalyst material. Because the amount of active catalyst in the film is decaying over time, the TOF value is an apparent, averaged estimation.

Material characterization. Thin-film structural properties were determined by X-ray diffraction under grazing incidence (GIXRD) conditions for crystallinity determination and phase detection with a PANalytical Empyrean equipment using Cu-Kα radiations. Thin-film morphologies were obtained using a Merlin VP Compact scanning electron microscope (SEM) provided by Zeiss, equipped with an energy dispersive X-Ray spectroscopy (EDS) detector from Bruker. Transmittance and Absorbance spectra were obtained using an Agilent Cary 5000 UV−Vis−NIR spectrophotometer equipped with an Agilent diffuse reflectance accessory. X-Ray Photoelectron Spectrometer analyses (XPS) were performed with a THERMO-VG ESCALAB 250 (RX source K AI (1486.6 eV)). Inductively coupled plasma (ICP) analyses were performed for the determination of the cobalt catalyst concentration into the films. The prepared thin layers were dissolved from the electrode using an acid solution 69% HNO_3. The resulting solution was then diluted to 2% HNO_3 and injected into a ICAP 6300 Thermoelectron apparatus with detection of cobalt (238.8 nm).

Chemical characterization. NMR spectrum was recorded in DMSO-d_6 on a Varian 500 MHz spectrometer. Infrared spectra (FT-IR) were recorded on a Bio-Rad FTS 175C FTIR

spectrophotometer. UV-visible absorption spectra were obtained using a Shimadzu 2001 UV spectrophotometer. High resolution mass spectra were measured on an Agilent 6530 Accurate-Mass Q-TOF LC/MS spectrometer equipped with electrospray ionization (ESI) source.

Supporting Information. Complementary characterization of ZnO layers (SEM, UV-Vis, EDX, XPS, AT-IR), Cyclic voltammetry and CPE experiments, Characterization of catalytic electrodes before and after electrolysis (Zn LMM Auger spectra, XRD), Catalyst synthesis characterizations (FT-IR, ^{1}H NMR, Uv-Vis).

Author information

Corresponding Authors

Umit Isci – Marmara University, Faculty of Technology, Department of Metallurgical & Materials Engineering, 34722 Istanbul, Türkiye; Email: umit.isci@marmara.edu.tr

Negar Naghavi – Institut Photovoltaïque d'Île-de-France (IPVF), CNRS, UMR 9006, 91120 Palaiseau, France; Email: negar.naghavi@chimieparistech.psl.eu

Marc Robert – Université Paris Cité, Laboratoire d' Electrochimie Moléculaire, CNRS, F-75013 Paris, France; Institut Universitaire de France (IUF), F-75005 Paris, France. Email: robert@u-paris.fr

Authors

Julian Guerrero – Université Paris Cité, Laboratoire d' Electrochimie Moléculaire, CNRS, F-75013 Paris, France; Institut Photovoltaïque d'Île-de-France (IPVF), CNRS, UMR 9006, 91120 Palaiseau, France.

Nathanaelle Schneider – Institut Photovoltaïque d'Île-de-France (IPVF), CNRS, UMR 9006, 91120 Palaiseau, France.

Fabienne Dumoulin – Acıbadem Mehmet Ali Aydınlar University, Faculty of Engineering and Natural Sciences, Biomedical Engineering Department, 34752 Ataşehir, Istanbul, Türkiye

Daniel Lincot– Institut Photovoltaïque d'Île-de-France (IPVF), CNRS, UMR 9006, 91120 Palaiseau, France.

Author Contributions

The manuscript was written through contributions of all authors. All authors have given approval to the final version of the manuscript.

Notes

The authors declare no competing financial interest.

Acknowledgements

The authors are very grateful for the financial support from the CNRS through the 80|Prime program. M.R. acknowledges the Institut Universitaire de France (IUF) for partial financial support.

References

(1) Kayan, A. Inorganic-Organic Hybrid Materials and Their Adsorbent Properties. *Adv Compos Hybrid Mater* **2019**, *2* (1), 34–45. https://doi.org/10.1007/s42114-018-0073-y.

(2) Ananikov, V. P. Organic–Inorganic Hybrid Nanomaterials. *Nanomaterials* **2019**, *9* (9), 1197. https://doi.org/10.3390/nano9091197.

(3) Chongdar, S.; Bhattacharjee, S.; Bhanja, P.; Bhaumik, A. Porous Organic–Inorganic Hybrid Materials for Catalysis, Energy and Environmental Applications. *Chem. Commun.* **2022**, *58* (21), 3429–3460. https://doi.org/10.1039/D1CC06340E.

(4) Sun, Y.; Wang, F.; Fu, Y.; Chen, C.; Wang, X.; Xiao, Z.; Liu, Y.; Xu, J.; Li, B.; Wang, L. Two New Inorganic–Organic Hybrid Zinc Phosphites and Their Derived ZnO/ZnS Heterostructure for Efficient Photocatalytic Hydrogen Production. *RSC Adv.* **2020**, *10* (2), 812–817. https://doi.org/10.1039/C9RA06919D.

(5) Li, M.; Garg, S.; Chang, X.; Ge, L.; Li, L.; Konarova, M.; Rufford, T. E.; Rudolph, V.; Wang, G. Toward Excellence of Transition Metal-Based Catalysts for CO_2 Electrochemical Reduction: An Overview of Strategies and Rationales. *Small Methods* **2020**, *4* (7), 2000033. https://doi.org/10.1002/smtd.202000033.

(6) Li, T.-T.; Mei, Y.; Li, H.; Qian, J.; Wu, M.; Zheng, Y.-Q. Highly Selective and Active Electrochemical Reduction of CO_2 to CO on a Polymeric Co(II) Phthalocyanine@Graphitic Carbon Nitride Nanosheet–Carbon Nanotube Composite. *Inorg. Chem.* **2020**, *59* (19), 14184–14192. https://doi.org/10.1021/acs.inorgchem.0c01977.

(7) Kinzel, N. W.; Werlé, C.; Leitner, W. Transition Metal Complexes as Catalysts for the Electroconversion of CO_2 : An Organometallic Perspective. *Angew. Chem. Int. Ed.* **2021**, anie.202006988. https://doi.org/10.1002/anie.202006988.

(8) Leung, C.-F.; Ho, P.-Y. Molecular Catalysis for Utilizing CO_2 in Fuel Electro-Generation and in Chemical Feedstock. *Catalysts* **2019**, *9* (9), 760. https://doi.org/10.3390/catal9090760.

(9) Dalle, K. E.; Warnan, J.; Leung, J. J.; Reuillard, B.; Karmel, I. S.; Reisner, E. Electro- and Solar-Driven Fuel Synthesis with First Row Transition Metal Complexes. *Chem. Rev.* **2019**, *119* (4), 2752–2875. https://doi.org/10.1021/acs.chemrev.8b00392.

(10) Wang, M.; Torbensen, K.; Salvatore, D.; Ren, S.; Joulié, D.; Dumoulin, F.; Mendoza, D.; Lassalle-Kaiser, B.; Işci, U.; Berlinguette, C. P.; Robert, M. CO_2 Electrochemical Catalytic Reduction with a Highly Active Cobalt Phthalocyanine. *Nat Commun* **2019**, *10* (1), 3602. https://doi.org/10.1038/s41467-019-11542-w.

(11) Ren, S.; Joulié, D.; Salvatore, D.; Torbensen, K.; Wang, M.; Robert, M.; Berlinguette, C. P. Molecular Electrocatalysts Can Mediate Fast, Selective CO_2 Reduction in a Flow Cell. **2019**, 4.

(12) Cheng, D.; Zhao, Z.-J.; Zhang, G.; Yang, P.; Li, L.; Gao, H.; Liu, S.; Chang, X.; Chen, S.; Wang, T.; Ozin, G. A.; Liu, Z.; Gong, J. The Nature of Active Sites for Carbon Dioxide Electroreduction over Oxide-Derived Copper Catalysts. *Nat Commun* **2021**, *12* (1), 395. https://doi.org/10.1038/s41467-020-20615-0.

(13) Pander, J. E.; Ren, D.; Huang, Y.; Loo, N. W. X.; Hong, S. H. L.; Yeo, B. S. Understanding the Heterogeneous Electrocatalytic Reduction of Carbon Dioxide on Oxide-Derived Catalysts. *ChemElectroChem* **2018**, *5* (2), 219–237. https://doi.org/10.1002/celc.201701100.

(14) Dattila, F.; García-Muelas, R.; López, N. Active and Selective Ensembles in Oxide-Derived Copper Catalysts for CO_2 Reduction. *ACS Energy Lett.* **2020**, *5* (10), 3176–3184. https://doi.org/10.1021/acsenergylett.0c01777.

(15) Verdaguer-Casadevall, A.; Li, C. W.; Johansson, T. P.; Scott, S. B.; McKeown, J. T.; Kumar, M.; Stephens, I. E. L.; Kanan, M. W.; Chorkendorff, I. Probing the Active Surface Sites for CO Reduction on Oxide-Derived Copper Electrocatalysts. *J. Am. Chem. Soc.* **2015**, *137* (31), 9808–9811. https://doi.org/10.1021/jacs.5b06227.

(16) Kostecki, R.; Augustynski, J. Electrochemical Reduction of CO_2 at an Activated Silver Electrode. *Berichte der Bunsengesellschaft für physikalische Chemie* **1994**, *98* (12), 1510–1515. https://doi.org/10.1002/bbpc.19940981203.

(17) Ma, M.; Trześniewski, B. J.; Xie, J.; Smith, W. A. Selective and Efficient Reduction of Carbon Dioxide to Carbon Monoxide on Oxide-Derived Nanostructured Silver Electrocatalysts. *Angew. Chem. Int. Ed.* **2016**, *55* (33), 9748–9752. https://doi.org/10.1002/anie.201604654.

(18) Bi, Q.; Huang, X.; Yin, G.; Chen, T.; Du, X.; Cai, J.; Xu, J.; Liu, Z.; Han, Y.; Huang, F. Cooperative Catalysis of Nickel and Nickel Oxide for Efficient Reduction of CO_2 to CH_4. *ChemCatChem* **2019**, *11* (4), 1295–1302. https://doi.org/10.1002/cctc.201801896.

(19) Wang, Z.; Fan, Jiajie; Cheng, Bei; Yu, Jiaguo; Xu, Jingsan. Nickel-Based Cocatalysts for Photocatalysis: Hydrogen Evolution, Overall Water Splitting and CO_2 Reduction. *Materials Today Physics* **2020**, *15*, 27. https://doi.org/10.1016/j.mtphys.2020.100279.

(20) Dey, G. R.; Belapurkar, A. D.; Kishore, K. Photo-Catalytic Reduction of Carbon Dioxide to Methane Using TiO_2 as Suspension in Water. *Journal of Photochemistry and Photobiology A: Chemistry* **2004**, *163* (3), 503–508. https://doi.org/10.1016/j.jphotochem.2004.01.022.

(21) Shehzad, N.; Tahir, M.; Johari, K.; Murugesan, T.; Hussain, M. A Critical Review on TiO_2 Based Photocatalytic CO_2 Reduction System: Strategies to Improve Efficiency. *Journal of CO_2 Utilization* **2018**, *26*, 98–122. https://doi.org/10.1016/j.jcou.2018.04.026.

(22) Jin, L.; Shaaban, E.; Bamonte, S.; Cintron, D.; Shuster, S.; Zhang, L.; Li, G.; He, J. Surface Basicity of Metal@TiO_2 to Enhance Photocatalytic Efficiency for CO_2 Reduction. *ACS Appl. Mater. Interfaces* **2021**, *13* (32), 38595–38603. https://doi.org/10.1021/acsami.1c09119.

(23) Djurišić, A. B.; Leung, Y. H. Optical Properties of ZnO Nanostructures. *Small* **2006**, *2* (8–9), 944–961. https://doi.org/10.1002/smll.200600134.

(24) Rezaie, M. N.; Mohammadnejad, S.; Ahadzadeh, S. Hybrid Inorganic-Organic Light-Emitting Heterostructure Devices Based on ZnO. *Optics & Laser Technology* **2021**, *138*, 106896. https://doi.org/10.1016/j.optlastec.2020.106896.

(25) Kao, M.-C.; Chen, H.-Z.; Young, S.-L.; Lin, C.-C.; Kung, C.-Y. Structure and Photovoltaic Properties of ZnO Nanowire for Dye-Sensitized Solar Cells. *Nanoscale Res Lett* **2012**, *7* (1), 260. https://doi.org/10.1186/1556-276X-7-260.

(26) Manor, A.; Katz, E. A.; Tromholt, T.; Krebs, F. C. Enhancing Functionality of ZnO Hole Blocking Layer in Organic Photovoltaics. *Solar Energy Materials and Solar Cells* **2012**, *98*, 491–493. https://doi.org/10.1016/j.solmat.2011.11.026.

(27) Sharma, A.; Franklin, J. B.; Singh, B.; Andersson, G. G.; Lewis, D. A. Electronic and Chemical Properties of ZnO in Inverted Organic Photovoltaic Devices. *Organic Electronics* **2015**, *24*, 131–136. https://doi.org/10.1016/j.orgel.2015.05.032.

(28) Luo, W.; Zhang, Q.; Zhang, J.; Moioli, E.; Zhao, K.; Züttel, A. Electrochemical Reconstruction of ZnO for Selective Reduction of CO_2 to CO. *Applied Catalysis B: Environmental* **2020**, *273*, 119060. https://doi.org/10.1016/j.apcatb.2020.119060.

(29) Han, K.; Ngene, P.; Jongh, P. Structure Dependent Product Selectivity for CO_2 Electroreduction on ZnO Derived Catalysts. *ChemCatChem* **2021**, *13* (8), 1998–2004. https://doi.org/10.1002/cctc.202001710.

(30) Raula, M.; Rashid, Md. H.; Paira, T. K.; Dinda, E.; Mandal, T. K. Ascorbate-Assisted Growth of Hierarchical ZnO Nanostructures: Sphere, Spindle, and Flower and Their Catalytic Properties. *Langmuir* **2010**, *26* (11), 8769–8782. https://doi.org/10.1021/la904507q.

(31) Kumar, S.; Kumar, A.; Kumar, A.; Krishnan, V. Nanoscale Zinc Oxide Based Heterojunctions as Visible Light Active Photocatalysts for Hydrogen Energy and Environmental Remediation. *Catalysis Reviews* **2020**, *62* (3), 346–405. https://doi.org/10.1080/01614940.2019.1684649.

(32) Jiang, X.; Cai, F.; Gao, D.; Dong, J.; Miao, S.; Wang, G.; Bao, X. Electrocatalytic Reduction of Carbon Dioxide over Reduced Nanoporous Zinc Oxide. *Electrochemistry Communications* **2016**, *68*, 67–70. https://doi.org/10.1016/j.elecom.2016.05.003.

(33) Jehl, Z.; Rousset, J.; Donsanti, F.; Renou, G.; Naghavi, N.; Lincot, D. Electrodeposition of ZnO Nanorod Arrays on ZnO Substrate with Tunable Orientation and Optical

Properties. *Nanotechnology* **2010**, *21* (39), 395603. https://doi.org/10.1088/0957-4484/21/39/395603.

(34) Pauporté, Th.; Bataille, G.; Joulaud, L.; Vermersch, F. J. Well-Aligned ZnO Nanowire Arrays Prepared by Seed-Layer-Free Electrodeposition and Their Cassie−Wenzel Transition after Hydrophobization. *J. Phys. Chem. C* **2010**, *114* (1), 194–202. https://doi.org/10.1021/jp9087145.

(35) Choi, K.-S.; Chang, S.-P. Effect of Structure Morphologies on Hydrogen Gas Sensing by ZnO Nanotubes. *Materials Letters* **2018**, *230*, 48–52. https://doi.org/10.1016/j.matlet.2018.07.031.

(36) Pelicano, C. M.; Yanagi, H. Enhanced Charge Transport in Al-Doped ZnO Nanotubes Designed *via* Simultaneous Etching and Al Doping of H_2O-Oxidized ZnO Nanorods for Solar Cell Applications. *J. Mater. Chem. C* **2019**, *7* (16), 4653–4661. https://doi.org/10.1039/C9TC00401G.

(37) Kim, K.; Choi, P. gyu; Itoh, T.; Masuda, Y. Atomic Step Formation on Porous ZnO Nanobelts: Remarkable Promotion of Acetone Gas Detection up to the Parts per Trillion Level. *J. Mater. Chem. A* **2022**, *10* (26), 13839–13847. https://doi.org/10.1039/D2TA02789E.

(38) Hong, M.; Meng, J.; Yu, H.; Du, J.; Ou, Y.; Liao, Q.; Kang, Z.; Zhang, Z.; Zhang, Y. Ultra-Stable ZnO Nanobelts in Electrochemical Environments. *Mater. Chem. Front.* **2021**, *5* (1), 430–437. https://doi.org/10.1039/D0QM00709A.

(39) Taunk, P. B.; Das, R.; Bisen, D. P.; Tamrakar, R. K.; Rathor, N. Synthesis and Optical Properties of Chemical Bath Deposited ZnO Thin Film. *Karbala International Journal of Modern Science* **2015**, *1* (3), 159–165. https://doi.org/10.1016/j.kijoms.2015.11.002.

(40) Sánchez-Martín, S.; Olaizola, S. M.; Castaño, E.; Urionabarrenetxea, E.; Mandayo, G. G.; Ayerdi, I. Study of Deposition Parameters and Growth Kinetics of ZnO Deposited by

Aerosol Assisted Chemical Vapor Deposition. *RSC Adv.* **2021**, *11* (30), 18493–18499. https://doi.org/10.1039/D1RA03251H.

(41) Nozik, A.J. Photoelectrochemical cells. *Phil. Trans. R. Soc. Lond. A*. ***1980.*** *295.* 453-470. http://doi.org/10.1098/rsta.1980.0141

(42) Peulon, S.; Lincot, D. Cathodic Electrodeposition from Aqueous Solution of Dense or Open-Structured Zinc Oxide Films. *Adv. Mater.* **1996**, *8* (2), 166–170. https://doi.org/10.1002/adma.19960080216.

(43) Izaki, M.; Omi, T. Transparent Zinc Oxide Films Prepared by Electrochemical Reaction. *Appl. Phys. Lett.* **1996**, *68* (17), 2439–2440. https://doi.org/10.1063/1.116160.

(44) Yoshida, T.; Minoura, H. Electrochemical Self-Assembly of Dye-Modified Zinc Oxide Thin Films. *Adv. Mater.* **2000**, No. 16, 4. https://doi.org/10.1002/1521-4095(200008)12:16<1219::AID-ADMA1219>3.0.CO;2-5

(45) Haller, S.; Suguira, T.; Lincot, D.; Yoshida, T. Design of a Hierarchical Structure of ZnO by Electrochemistry for ZnO-Based Dye-Sensitized Solar Cells: Design of a Hierarchical Structure of ZnO by Electrochemistry. *phys. stat. sol. (a)* **2010**, *207* (10), 2252–2257. https://doi.org/10.1002/pssa.201026140.

(46) Yoshida, T.; Tochimoto, M.; Schlettwein, D.; Wöhrle, D.; Sugiura, T.; Minoura, H. Self-Assembly of Zinc Oxide Thin Films Modified with Tetrasulfonated Metallophthalocyanines by One-Step Electrodeposition. *Chem. Mater.* **1999**, *11* (10), 2657–2667. https://doi.org/10.1021/cm980619o.

(47) Pauporté, T.; Yoshida, T.; Cortès, R.; Froment, M.; Lincot, D. Electrochemical Growth of Epitaxial Eosin/ZnO Hybrid Films. *J. Phys. Chem. B* **2003**, *107* (37), 10077–10082. https://doi.org/10.1021/jp034079g.

(48) Pauporté, T.; Bedioui, F.; Lincot, D. Nanostructured Zinc Oxide–Chromophore Hybrid Films with Multicolored Electrochromic Properties. *J. Mater. Chem.* **2005**, *15* (15), 1552–1559. https://doi.org/10.1039/B416419A.

(49) Yang, H.; Wang, X.; Hu, Q.; Chai, X.; Ren, X.; Zhang, Q.; Liu, J.; He, C. Recent Progress in Self-Supported Catalysts for CO_2 Electrochemical Reduction. *Small Methods* **2020**, *4* (6), 1900826. https://doi.org/10.1002/smtd.201900826.

(50) Basnet, P.; Samanta, D.; Inakhunbi Chanu, T.; Mukherjee, J.; Chatterjee, S. Assessment of Synthesis Approaches for Tuning the Photocatalytic Property of ZnO Nanoparticles. *SN Appl. Sci.* **2019**, *1* (6), 633. https://doi.org/10.1007/s42452-019-0642-x.

(51) Höchst, H.; Goldmann, A.; Hüfner, S.; Malter, H. X-Ray Photoelectron Valence Band Studies on Phthalocyanine Compounds. *Physica Status Solidi b,* **1976**, 76. 559-586. https://doi.org/10.1002/pssb.2220760215

(52) Hellgren, N.; Guo, J.; Luo, Y.; Såthe, C.; Agui, A.; Kashtanov, S.; Nordgren, J.; Ågren, H.; Sundgren, J.-E. Electronic Structure of Carbon Nitride Thin Films Studied by X-Ray Spectroscopy Techniques. *Thin Solid Films* **2005**, *471* (1–2), 19–34. https://doi.org/10.1016/j.tsf.2004.03.027.

(53) Neelgund, G. M.; Oki, A. Cobalt Phthalocyanine-Sensitized Graphene–ZnO Composite: An Efficient Near-Infrared-Active Photothermal Agent. *ACS Omega* **2019**, *4* (3), 5696–5704. https://doi.org/10.1021/acsomega.8b03222.

(54) Luo, W.; Zhang, Q.; Zhang, J.; Moioli, E.; Zhao, K.; Züttel, A. Electrochemical Reconstruction of ZnO for Selective Reduction of CO_2 to CO. *Applied Catalysis B: Environmental* **2020**, *273*, 119060. https://doi.org/10.1016/j.apcatb.2020.119060.

(55) Geng, Z.; Kong, X.; Chen, W.; Su, H.; Liu, Y.; Cai, F.; Wang, G.; Zeng, J. Oxygen Vacancies in ZnO Nanosheets Enhance CO_2 Electrochemical Reduction to CO. *Angew. Chem.* **2018**, *130* (21), 6162–6167. https://doi.org/10.1002/ange.201711255.

(56) Xiang, Q.; Li, F.; Wang, J.; Chen, W.; Miao, Q.; Zhang, Q.; Tao, P.; Song, C.; Shang, W.; Zhu, H.; Deng, T.; Wu, J. Heterostructure of ZnO Nanosheets/Zn with a Highly Enhanced Edge Surface for Efficient CO_2 Electrochemical Reduction to CO. *ACS Appl. Mater. Interfaces* **2021**, *13* (9), 10837–10844. https://doi.org/10.1021/acsami.0c20302.

(57) Liu, K.; Wang, J.; Shi, M.; Yan, J.; Jiang, Q. Simultaneous Achieving of High Faradaic Efficiency and CO Partial Current Density for CO_2 Reduction via Robust, Noble-Metal-Free Zn Nanosheets with Favorable Adsorption Energy. *Adv. Energy Mater.* **2019**, *9* (21), 1900276. https://doi.org/10.1002/aenm.201900276.

(58) Zong, X.; Jin, Y.; Li, Y.; Zhang, X.; Zhang, S.; Xie, H.; Zhang, J.; Xiong, Y. Morphology-Controllable ZnO Catalysts Enriched with Oxygen-Vacancies for Boosting CO2 Electroreduction to CO. *Journal of CO_2 Utilization* **2022**, *61*, 102051. https://doi.org/10.1016/j.jcou.2022.102051.

(59) Zhang, X.; Wu, Z.; Zhang, X.; Li, L.; Li, Y.; Xu, H.; Li, X.; Yu, X.; Zhang, Z.; Liang, Y.; Wang, H. Highly Selective and Active CO_2 Reduction Electrocatalysts Based on Cobalt Phthalocyanine/Carbon Nanotube Hybrid Structures. *Nat Commun* **2017**, *8* (1), 14675. https://doi.org/10.1038/ncomms14675.

(60) Mai, N. T.; Thuy, T. T.; Mott, D. M.; Maenosono, S. Chemical Synthesis of Blue-Emitting Metallic Zinc Nano-Hexagons. *CrystEngComm* **2013**, *15* (33), 6606. https://doi.org/10.1039/c3ce40801a.

(61) Le Tulzo, H.; Schneider, N.; Lincot, D.; Patriarche, G.; Donsanti, F. Impact of the Sequence of Precursor Introduction on the Growth and Properties of Atomic Layer Deposited Al-Doped ZnO Films. *Journal of Vacuum Science & Technology A* **2018**, *36* (4), 041502. https://doi.org/10.1116/1.5030990.

(62) König, M.; Vaes, J.; Klemm, E.; Pant, D. Solvents and Supporting Electrolytes in the Electrocatalytic Reduction of CO_2. *iScience* **2019**, *19*, 135–160. https://doi.org/10.1016/j.isci.2019.07.014.

(63) Pati, P. B.; Wang, R.; Boutin, E.; Diring, S.; Jobic, S.; Barreau, N.; Odobel, F.; Robert, M. Photocathode Functionalized with a Molecular Cobalt Catalyst for Selective Carbon Dioxide Reduction in Water. *Nat Commun* **2020**, *11* (1), 3499. https://doi.org/10.1038/s41467-020-17125-4.